PERGAMON

International Journal of Heat and Mass Transfer 42 (1999) 3291–3306

International Journal of HEAT and MASS TRANSFER

Non-isothermal laminar flow and heat transfer between disks corotating in a fixed enclosure

Joan Herrero[a], Fransesc Giralt[a], Joseph A.C. Humphrey[b,*]

[a]*Departament d'Enginyeria Química, Universitat Rovira i Virgili de Tarragona, Autovia Salou, s/n, 43006 Tarragona, Catalunya, Spain*

[b]*College of Engineering, Bucknell University, Lewisburg, PA 17837, USA*

Received 24 July 1998; received in revised form 17 November 1998

Abstract

This is a numerical investigation of the coupled laminar flow and heat transfer in the space between a pair of disks attached to a hub rotating about a vertical axis in a fixed cylindrical enclosure. A temperature variation is imposed in the fluid by setting the disks at different uniform temperatures, the temperature of the bottom disk being higher than that of the top disk. The Boussinesq approximation is used to characterize buoyancy forces in the momentum conservation equations.

The different types of interdisk flow that arise as a function of angular velocity are described. At low Reynolds numbers the flow is primarily driven by gravity-induced buoyancy. As the Reynolds number increases, free convection yields to centrifugally-induced buoyancy. At sufficiently high Reynolds numbers, convection patterns induced by the strong shear at the enclosure wall dominate the interdisk flow and heat transfer but centrifugal buoyancy continues to influence the 3-D flow structure with respect to the isothermal case. One of the effects of buoyancy is the appearance of a new transition in the bifurcation diagram previously investigated by the authors for the isothermal flow case. Here, centrifugal buoyancy favors the generation of a 3-D flow which features a strong breaking of its symmetry properties with respect to the interdisk midplane, as in the isothermal case.

Heat transfer rates are calculated for a range of Reynolds numbers and interdisk spacings. Special attention is paid to the high Reynolds number forced convection regime which is of practical interest. It is shown that the scales derived from heat and mass transfer analyses of the freely rotating disk apply to the present problem. In many of the present cases, 2-D (axisymmetric) and 3-D calculations yield very similar values for the overall heat transfer rates. This is especially the case for those flows with a wavy 3-D structure, meaning flows which, on average, are symmetrical with respect to the interdisk midplane. However, examples are also provided where the flow is strongly 3-D, requiring computationally intensive calculations to obtain accurate predictions of the corresponding heat transfer rates.

1. Introduction

The main objective of this investigation is to analyze the effect of buoyancy forces on the basic structure of the laminar flow in the space between a pair of disks corotating in a fixed cylindrical enclosure. This is done by numerically solving the coupled momentum and energy equations for the case of an incompressible, non-isothermal fluid. The isothermal flow case was previously investigated by the authors [1] for the enclosed corotating disk pair (ECDP) geometry. Here attention

* Corresponding author.

0017-9310/99/$ - see front matter
PII: S0017-9310(98)00383-4

Nomenclature

Ac	acceleration ratio, $g/\Omega^2 R_2$
g	acceleration of gravity
h	local heat transfer coefficient, Eq. (11)
H	interdisk spacing
k	fluid thermal conductivity
L	length of the square side in the benchmark problem of Section 3
n_x, n_y	number of calculation nodes in the benchmark problem of Section 3
Nu, $\overline{Nu}$	local and average Nusselt numbers, Eqs. (10) and (11)
P, P', P''	dimensional, modified, and non-dimensional pressure, see Eqs. (1) and (2)
Pr	Prandtl number, ν/α
q	heat flux at the disk surface, Eq. (11)
r'	non-dimensional radial coordinate $(r-R_1)/(R_2-R_1)$
r, R	dimensional and non-dimensional radial coordinate, see Eq. (3)
Ra	Rayleigh number, $g\varepsilon H^3/\nu\alpha$
Ra_c	critical Rayleigh number for the onset of Rayleigh–Bénard convection
Ra_Ω	rotational Rayleigh number, $Re^2\ \varepsilon\ Pr=\Omega^2\varepsilon R_2^4/\nu\alpha$
Re	Reynolds number, $\Omega R_2^2/\nu$
R_1, R_2	internal and external disk radius, respectively
S	height to radius space ratio, H/R_2
t	time
Ta	Taylor number, $4\Omega^2 H^4/\nu^2$
T, T_0	local and bulk fluid temperature, respectively
T_b, T_t	temperature of the bottom and top disks, respectively
T_s	temperature at the disk surface
u, U	dimensional and non-dimensional axial velocity component, see Eq. (3)
T'	dimensionless fluid temperature, see Eq. (3)
v, V	dimensional and non-dimensional radial velocity component, see Eq. (3)
w, W	dimensional and non-dimensional circumferential velocity component, see Eq. (3)
z, Z	dimensional and non-dimensional axial coordinate, see Eq. (3).

Greek symbols

α	fluid thermal diffusivity
β	thermal expansion coefficient
ε	thermal Rossby number, $\beta(T_b-T_t)$
θ	circumferential coordinate (radians)
λ	wavelength of the Rayleigh–Bénard rolls, defined as the ratio between twice the average roll width and H
λ_c	wavelength of the rolls at the onset of Rayleigh–Bénard convection
ν	fluid kinematic viscosity
ρ, ρ_0	local and bulk fluid density, respectively
τ	non-dimensional time, Eq. (3)
Ω	angular velocity of the disks and hub.

is paid to the scaling and prediction of heat transfer rates for a range of conditions of practical interest, including high speeds of rotation. A sketch of the configuration investigated is shown in Fig. 1. The geometry and boundary conditions match those considered in [1] except for the imposition of a temperature variation by setting the bottom and top disks at uniform temperatures T_b and T_t, respectively, with $T_b > T_t$, while treating the cylindrical wall as adiabatic. It should be noted that the present problem is different from the non-isothermal flow in a rotating cavity or in rotor-stator systems both of which have been thoroughly investigated in recent years [2–5].

The effect of moderate buoyancy forces on ECDP flow will be assessed within the range of Reynolds numbers $0 \leqslant Re \leqslant 10^5$, approximately. With reference to

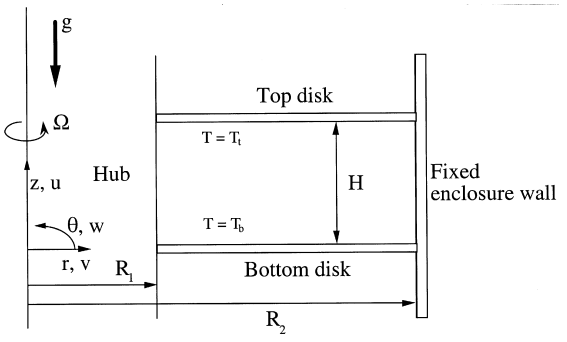

Fig. 1. Schematic of the geometry investigated. In all the cases $R_2/R_1 = 1.862$. The bottom disk ($z = 0$) is set at a uniform temperature T_b higher than that of the top disk, T_t, and the initial bulk fluid temperature is taken as $T_0 = 300$ K.

Fig. 1, the Reynolds number is defined as $Re = \Omega R_2^2/\nu$, where R_2 is the disk radius, Ω is the angular velocity of the disks and hub, and ν is the kinematic viscosity of the fluid. The Boussinesq approximation is employed in the conservation equations. Results cover the interdisk space ratio range, $0.05 \leqslant S = H/R_2 \leqslant 0.20$, with special attention paid to $S = 0.091$ because it has been widely studied in the literature on ECDP flows [6–8].

Different flow regimes and heat transfer characteristics are expected for different ranges of the Reynolds number, depending on which terms dominate the conservation equations. At very low Reynolds numbers, free convection, usually known as Rayleigh–Bénard convection for unstably stratified flows, arises in the form of an organized cross-stream motion which significantly increases the heat transfer rate. Literature reviews on Rayleigh–Bénard convection are available in the literature; see, for example, Koschmieder [9]. Only some relevant aspects of the subject are considered in Section 4.1 to establish the proper comparisons. It is well-known that Rayleigh–Bénard convection decays as rotation increases [10]. As discussed in Section 4.2, such decay is accompanied by the appearance of both centrifugally-induced buoyancy and a strong shear at the enclosure wall. It is the wall-shearing of the fluid that induces the cross-stream motion typical of the isothermal ECDP flow [6].

Beyond a certain value of the Reynolds number, free convection effects become negligible and one should observe the main characteristics of isothermal ECDP flow. Non-isothermal ECDP flow has been investigated by the authors [11] in a range of Reynolds numbers where the flow remained axisymmetric (2-D). They showed that centrifugally-induced buoyancy exerts significant effects on the structure of the flow. As in the isothermal case, increasing the Reynolds number leads to the transition from a 2-D to a 3-D non-isothermal ECDP flow, discussed in Section 4.3 below. However, it has been shown recently [1] that the isothermal 3-D ECDP flow has one of two structures, depending on the values of S and Re. Such a distinction also holds here for the non-isothermal flow and is relevant to the prediction of heat transfer rates as shown in Sections 4.4 and 4.5.

The remainder of this paper is divided as follows. The conservation equations and relevant characteristic scales are presented in Section 2. The main features of the numerical algorithm and the effects of grid size on the accuracy of the calculations are discussed in Section 3. Results for the different flow regimes outlined above are presented in Sections 4.1–4.4. Predicted heat transfer rates are presented in Section 4.5 where they are compared to previous analysis. The effects of the aspect ratio, S, and the Prandtl number on the interdisk heat transfer are also discussed in Section 4.5. Conclusions are given in Section 5.

2. Conservation equations and scaling

For purposes of calculation, the fluid is assumed to be incompressible and Newtonian and the effect of density variation is accounted for through the Boussinesq approximation [12]. It is especially convenient in the present case to write the conservation equations in the rotating frame of reference, as additional buoyancy forces arise from the interaction between inertial forces and density gradients. By defining the modified pressures

$$P' = P - \rho_0 g z \tag{1}$$

$$P'' = (P' - 1/2\Omega^2 R_2^2)/\rho_0 \Omega^2 R_2^2 \tag{2}$$

and the dimensionless variables

$$U = u/\Omega R_2; \quad V = v/\Omega R_2; \quad W = w/\Omega R_2;$$
$$T' = (T - T_0)/\Delta T; \quad Z = z/R_2; \quad R = r/R_2; \tag{3}$$
$$\tau = \Omega t$$

the conservation equations for mass, momentum and energy may be written as

$$\frac{\partial U}{\partial Z} + \frac{\partial V}{\partial R} + \frac{V}{R} + \frac{1}{R}\frac{\partial W}{\partial \theta} = 0 \tag{4}$$

$$\frac{DU}{D\tau} = -\frac{\partial P''}{\partial Z} + \frac{1}{Re}\nabla^2 U + Ac\varepsilon T' \tag{5}$$

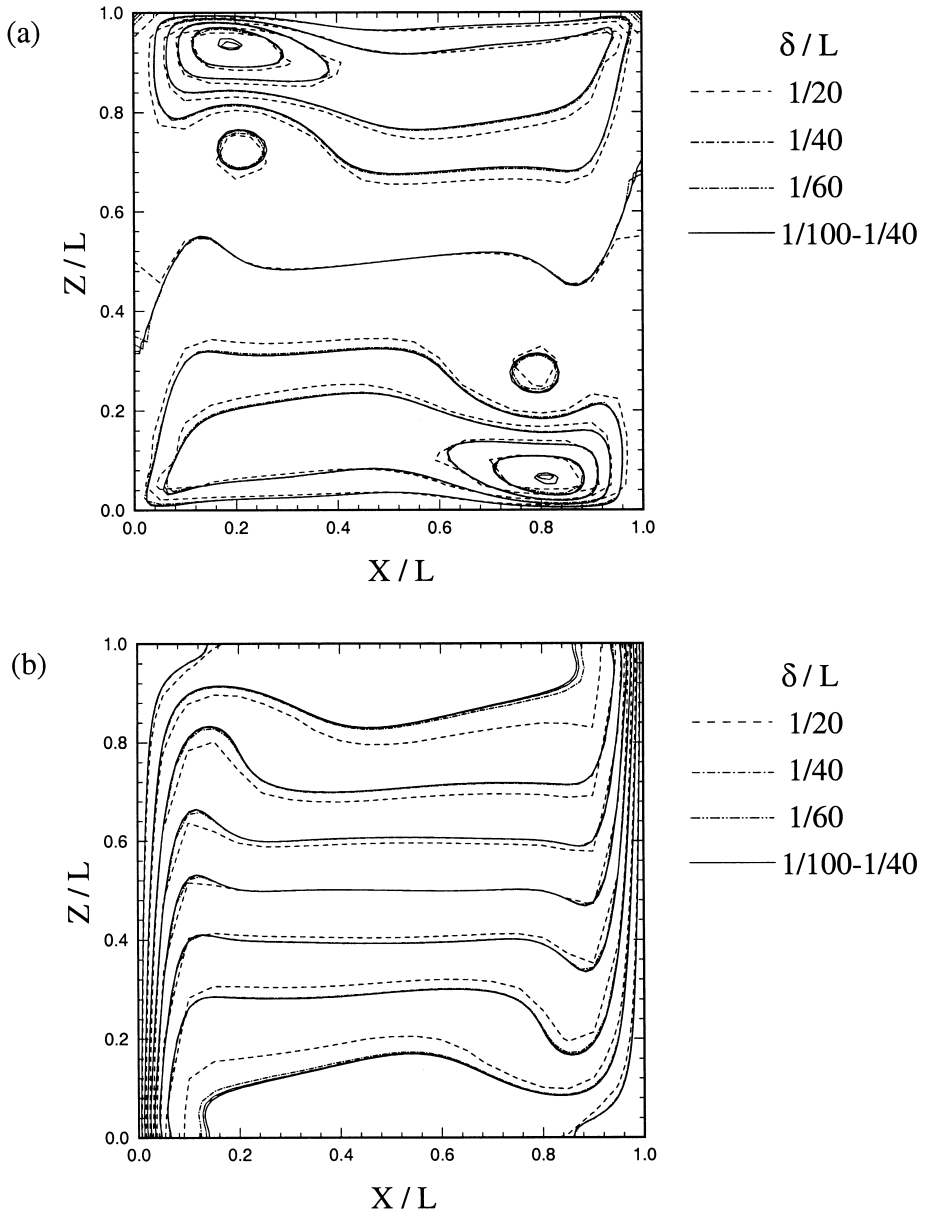

Fig. 2. Calculations on several grids for the test case consisting of a square enclosure heated along one vertical side for $Ra=10^6$. Three of the grids have a uniform spacing of $\delta/L=1/20$, 1/40 and 1/60, in order of increasing refinement. The most accurate predictions are obtained for a non-uniform grid with $n_x=n_y=61$. For this grid, the spacing grows linearly from a minimum of $\delta/L=0.01$ close to the wall up to a maximum of $\delta/L=0.025$. Calculated contours of the x-velocity component are presented in (a) while the corresponding temperature distributions are shown in (b).

$$\frac{DV}{D\tau}=-\frac{\partial P''}{\partial R}+\frac{1}{Re}\nabla^2 V-R\varepsilon T'+[1-\varepsilon T'](2W+W^2/R) \quad (6)$$

$$\frac{DW}{D\tau}=-\frac{\partial P''}{\partial \theta}+\frac{1}{Re}\nabla^2 W-[1-\varepsilon T'](2V+VW/R) \quad (7)$$

$$\frac{DT'}{D\tau}=\frac{1}{Re\,Pr}\nabla^2 T'. \quad (8)$$

In Eqs. (2)–(8), T_0 is the bulk fluid temperature, ρ_0 is the fluid density evaluated at the temperature T_0, Ω is the angular velocity of the disks and hub, and u, v, w are the respective velocity components in the axial (z), radial (r), and circumferential (θ) coordinate direc-

Table 1
Comparison of results on different grids with the benchmark solution presented by De Vahl Davis [16]. The Rayleigh number is $Ra=10^6$. The nomenclature and variable scaling are taken from [16]. The symbol %E refers to the percentage deviation of the quantities predicted with respect to the benchmark values reported in [16]

n	h/L	u_{max}	%E	w_{max}	%E	Nu_{av}	%E	Nu_{max}	%E
21	1/20	68.80	6.45	243.6	11.1	10.29	16.7	20.64	15.1
41	1/40	65.33	1.08	218.6	−0.35	9.046	2.60	19.69	9.85
61	1/60	64.94	0.48	217.3	−0.94	8.890	0.83	18.56	3.54
61	—	64.92	0.45	219.6	0.11	8.843	0.29	17.86	−0.36

tions. The Prandtl number is defined as the ratio between the fluid kinematic viscosity and thermal diffusivity, $Pr=\nu/\alpha$. The additional dimensionless group, $Ac=g/\Omega^2 R_2$, in Eq. (5) represents the ratio between the gravitational and centrifugal accelerations. Note that the mean centrifugal term in Eq. (6) has been incorporated into the modified pressure. The other force that arises in the rotating frame of reference is the Coriolis force, which couples the radial and circumferential components of motion. The linearization of the density in the source terms of Eqs. (5)–(7) leads to the explicit appearance of buoyancy forces. Note that in Eqs. (5)–(7) density is linearized not only in the gravity term but also in the Coriolis and centrifugal force terms. For a discussion of the conditions that guarantee the validity of the Boussinesq approximation the reader is directed to Gray and Giorgini [12] and Frölich et al. [13]. Because in this study the product $\varepsilon=\beta(T_b-T_t)$ is never larger (in absolute value) than $\varepsilon=0.1$, the approximation holds.

Relative to the rotating frame of reference, the boundary conditions used to solve Eqs. (4)–(8) are as follows:

$$u=0,\quad v=0 \text{ and } w=0 \text{ along all rotating surfaces} \tag{9a}$$

$$u=0,\quad v=0 \text{ and } w=-\Omega R_2 \text{ at the fixed enclosure wall} \tag{9b}$$

$$T=T_b \quad \text{for } z=0 \text{ (bottom disk)} \tag{9c}$$

$$T=T_t \quad \text{for } z=H \text{ (top disk)} \tag{9d}$$

$$(\partial T/\partial r)=0 \text{ for } r=R_1 \text{ and } r=R_2 \text{ (adiabatic hub and enclosure surfaces).} \tag{9e}$$

Note that when free convection dominates the flow and heat transfer, different scales must be used for the velocity vector and time, namely $\mathbf{V}=\mathbf{v}/(g\varepsilon H)^{1/2}$ and $\tau=t\alpha/H^2$ [9]. The Rayleigh number, commonly used in free convection studies, does not appear explicitly in Eqs. (5)–(8) but can be expressed as a combination of the dimensionless groups defined above ($Ra=Re^2\ Pr\ Ac\varepsilon S^3$). Another parameter used frequently in this type of flow is the Taylor number which can be expressed as $Ta=4\ Re^2\ S^2$. However, the rotational Rayleigh number, Ra_Ω, defined in the Nomenclature, should be used in flows dominated by centrifugal buoyancy, e.g., in rotating cavities [2]. Local and surface-averaged heat transfer rates are expressed in the form of the Nusselt number, $Nu=hH/k$, where k is the thermal conductivity of the fluid and h is the heat transfer coefficient, computed on the basis of either the local or the averaged temperature gradient at the disk surface.

3. Numerical method

Calculations have been carried out using the CUTEFLOWS numerical algorithm. The main features of the code are discussed in [1] and [8], where the numerical uncertainty associated with predicting isothermal ECDP flows is assessed. The code is second-order accurate in space and time and has been tested successfully with respect to two benchmark backward-facing step problems [14,15]. Even though these tests show the ability of the code to properly predict the flow and heat transfer in mixed convection problems, additional testing has been carried out to further guarantee the correctness of the present results. For this, the well-known problem of buoyancy-driven flow in a 2-D square enclosure has been selected. Benchmark results for this free convection problem have been reported by De Vahl Davis [16] whose nomenclature and scales are used to present the test results.

Figs. 2(a) and (b), respectively, show contours of the calculated horizontal velocity component and temperature on different grids for the most challenging case with a value of the Rayleigh number $Ra=10^6$. These plots show that even the coarsest grid, with a uniform spacing of $h/L=1/20$, yields qualitatively good results. A more quantitative comparison with De Vahl Davis' results is provided in Table 1. Except for the distri-

bution of the local heat transfer rates on the hot wall, a uniform grid with $h/L=1/60$ yields good results. At $Ra=10^6$ the wall boundary layers are very thin and the peak in the profile of the local Nusselt number occurs very near the horizontal wall. A different non-uniform arrangement of the $n_x=n_y=61$ nodes leads to improved predictions in Table 1. The key point is that the latter grid is fine enough near the wall, having five nodes embedded in the thermal boundary layer.

The requirement of a refined grid close to a solid boundary has been adopted in the present investigation in those calculations corresponding to the convection dominated regime, where the proper characterization of the disk Ekman layers is critical. The grids implemented in the present work to characterize the non-isothermal ECDP flow in the forced-convection regime are equivalent to those employed in [1] for the isothermal case. An exception is made for the calculations with Prandtl numbers higher than $Pr=0.76$. For these cases the asymptotic dependence of the thermal boundary layer thickness on $Pr^{1/3}$ is accounted for. As in [1], present calculations were generally started from the initial condition of a motionless fluid (in the fixed frame of reference) at a uniform temperature. The most intensive, 3-D calculations have generally been started from the corresponding previously calculated isothermal flow.

4. Results and discussion

Calculations have been carried out within the range of parameters $0\leqslant Re\leqslant 10^5$, $0.05\leqslant S\leqslant 0.2$, and $\varepsilon\leqslant 0.1$. The $(Ac\ Re^2)$ product was constant and equal to 674. Most of the results presented correspond to air with a Prandtl number $Pr=0.76$. Several calculations at higher values of Pr have also been carried out within the forced convection regime in order to establish the effect of the Prandtl number on the overall heat transfer rates. The different flow regimes observed as a function of the Reynolds number are analyzed in Sections 4.1–4.4 while the predicted heat transfer rates are discussed in Section 4.5.

4.1. The limit of zero rotation: Rayleigh–Bénard convection

Any rotation-dependent effects are obviously absent in the limit of $Re\rightarrow 0$ where only free convection, or Rayleigh–Bénard convection, drives the flow and heat transfer. The onset of free convection has been the subject of considerable research [9] and calculations of the flow near this condition are useful to further test the code. The typical roll pattern presented in Fig. 3(a) has been obtained in a calculation with $\varepsilon=0.1$ and $S=0.091$ ($Ra=2280$) on a uniformly spaced 40×74 (z, r) grid. For the sake of simplicity, only the axisymmetric mode of Rayleigh–Bénard convection has been considered. An analysis on the subject of the preferred mode at the onset of thermal convection in a cylindrical container may be found, for instance, in the paper by Buell and Catton [17]. The axisymmetric mode also presents the nice feature, shown by Chandrasekhar [10], that both the value of the critical Rayleigh number and the 2-D flow pattern at the onset are the same for any fluid, that is, they are independent of the Prandtl number. This critical value should be $Ra_c=1708$ in the limit of a very thin fluid layer ($S\rightarrow 0$).

The first question is whether the pattern of five rolls in Fig. 3(a) is appropriate for the conditions examined. Chandrasekhar showed that the average wave-length of the 2-D roll pattern at onset is $\lambda_c=2.016$. The slightly supercritical pattern ($Ra=2280>Ra_c$) of Fig. 3(a) yields $\lambda=2.04\pm 0.1$ by simple averaging, and $\lambda=2.07\pm 0.1$ using the correction for cylindrical geometries suggested by Koschmieder and Pallas [18]. Both values of λ are in good agreement with the theoretical one.

A second valuable point is the prediction of the critical Rayleigh number, Ra_c. It was found, for the geometry sketched in Fig. 1, that Rayleigh–Bénard convection first set in at about $Ra_c=1800$ for $S=0.091$. The analysis by Buell and Catton [17] suggests that the critical value should be considerably lower, about $1720\leqslant Ra_c\leqslant 1740$ for the axisymmetric mode, yet the use of much finer computational grids yielded no significant difference in the predicted Ra_c value. The reason for this apparent discrepancy is attributed to the fact that Buell and Catton dealt with the case of a cylinder; that is, $R_1=0$ in the context of Fig. 1. In support of this interpretation, calculations have also been performed for a geometry with $R_1=0$ and $S=0.097$, matching that in the experiments of Koschmieder [19]. The roll pattern at $Ra=1725$, the lowest Ra value at which free convection has been numerically detected in this set of runs with $R_1=0$, is shown in Fig. 3(b) for a calculation on a 40×100 (z, r) grid. The number of rolls is in agreement with the ten roll axisymmetric pattern reported by Koschmieder [19] at the onset of convection. More important, the predicted critical Rayleigh number approaches the theoretical limit for $S=0$ given by Chandrasekhar [10]. Thus, it is shown that the presence of an inner cylindrical wall has a stabilizing effect on the axisymmetric mode of thermal convection.

Another quantity commonly used to compare theory with experiments or calculations is the initial slope of the heat transfer curve, defined as $\{Ra(Nu-1)\}/(Ra-Ra_c)$ in studies of Rayleigh–Bénard convection. This is the value of the slope just beyond the onset of free convection. Schüler et al. [20] showed analytically

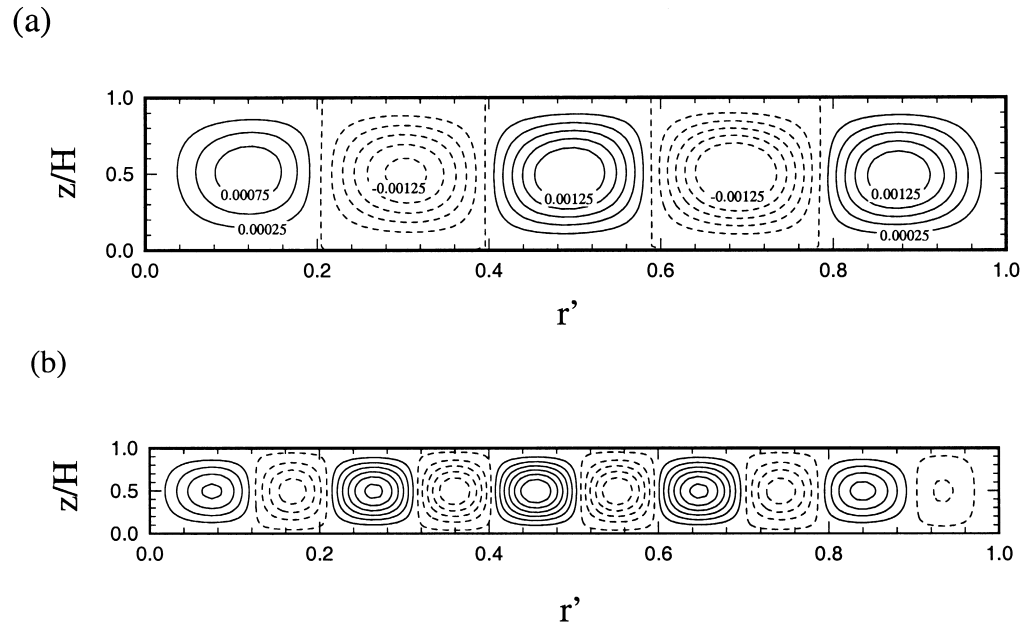

Fig. 3. Results for the zero rotation limit, $Re=0$. The Rayleigh–Bénard roll pattern obtained for the geometry of Fig. 1 in a 2-D calculation with $Pr=0.76$, $S=0.091$ and $Ra=2280$ is shown in (a). The axisymmetric solution obtained in the case of a cylindrical container with $R_1=0$, $Pr=0.76$, $S=0.097$ and $Ra=1710$ is shown in (b). The number of computational nodes used in these calculations is 40×74 and 40×100 (z, r), respectively. In both plots the stream-function is made dimensionless using a reference flow rate consisting of the product between the typical velocity scale, $(g\varepsilon H)^{1/2}$ and the disk surface area, $\pi(R_2^2-R_1^2)$.

that, for a steady 2-D roll pattern in a plane geometry, the initial slope of this curve depends on the Prandtl number and is equal to 1.39 for $Pr=0.76$. A value of the slope of 1.35, close to the theoretical prediction, is obtained in present calculations for the conditions of Fig. 3(a).

4.2. Mixed convection at low Reynolds numbers

The decay of free convection with increasing rotation is accompanied by a progressive increase of the shear stress in the vicinity of the fixed enclosure wall. As a consequence, the cross-stream pattern typical of ECDP flows, with two counter-rotating vortices near the outer wall [8], eventually emerges. Also, with increasing rotation centrifugal buoyancy sets in. The combined action of these two effects is reflected in the cross-stream flow patterns, respectively, shown in Figs. 4(a) and (b) for 2-D calculations with $Re=1371$ ($\Omega=20$ rpm) and $Re=2742$ carried out on 40×74 (z, r) grids.

When compared to the non-rotating case, Fig. 3(a), the strength of the Rayleigh–Bénard rolls has in general been dampened by the Coriolis force which opposes any radial motion [see Eq. (6)]. The centrifugal buoyancy term, as shown in previous experiments and analysis [19,21,22], favors clockwise cross-stream rotation and opposes anticlockwise cross-stream rotation. Note that the third roll in Fig. 4(a) retains the same strength as the third roll in Fig. 3(a), while the two anticlockwise rolls are considerably weaker. Note also in Fig. 4(a) that the effects of shear at the enclosure wall are already weakly present in the form of a small counter-clockwise roll that arises at the lower right corner. Such effects manifest themselves more clearly in the flow pattern of Fig. 4(b). The pair of counter-rotating cross-stream vortices near the outer cylindrical wall is already present in this plot. The Rayleigh–Bénard rolls have become very weak at $Re=2741$, to the point that only the two innermost rolls remain as independent entities in Fig. 4(b). The result of weakening free convection by increasing the disk speed of rotation is to progressively reduce the transport of heat from the bottom to the top disk. This is reflected in the shape of the heat transfer curve presented in Subsection 4.5.

4.3. Forced convection regime: wavy-3-D flows

When the Reynolds number is increased to values larger than about 10^5 for $S=0.091$, $Pr=0.76$, and $\varepsilon=0.1$, free convection vanishes and the characteristics of the resulting flow asymptote towards those of the isothermal ECDP case. Here we discuss how centrifug-

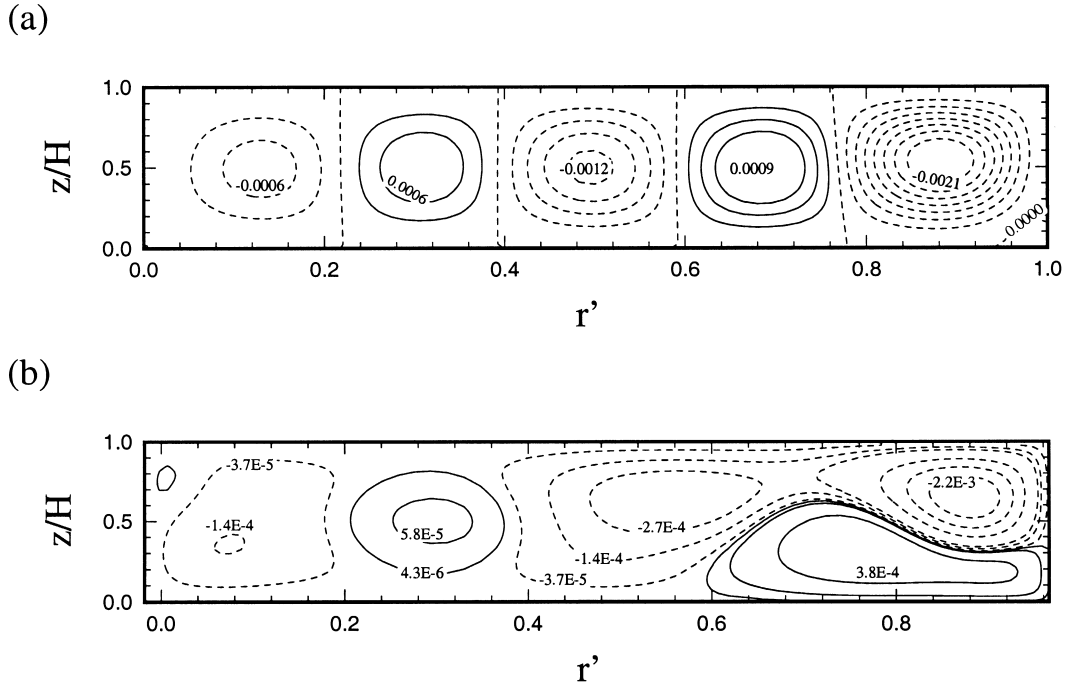

Fig. 4. Streamline patterns obtained in 2-D calculations on a 40×74 (z, r) grid for $Re = 1371$ (a) and $Re = 2742$ (b). Except for where otherwise indicated, in this and the following figures the flow parameters are $S = 0.091$, $\varepsilon = 0.1$ and $Pr = 0.76$. The stream function has been non-dimensionalized as explained in the caption to Fig. 3.

ally-induced buoyancy alters the basic 3-D structure of the isothermal ECDP flow. The results presented correspond to a unique value, $\varepsilon = 0.1$, of the dimensionless temperature difference. The present buoyancy-related effects are also observed, although to a lesser extent, in calculations with lower values of ε. As a general rule, the influence of centrifugal buoyancy decays linearly with decreasing ε.

As observed for the isothermal case [1,8,23], the buoyancy-affected axisymmetric (2-D) flow becomes 3-D at a large enough value of the Reynolds number. The presence of moderate buoyancy forces ($\varepsilon = 0.1$) produces very little change in the transition Reynolds number from 2-D-steady to 3-D-unsteady ECDP flows. The 3-D flow analyzed in this section corresponds to the type arising after a 2-D–3-D Hopf bifurcation, previously analyzed in the isothermal case by Humphrey et al. [8]. These authors reported a circumferentially periodic, 3-D ECDP flow, characterized by a circumferential waviness of the pair of ECDP cross-stream vortices. These vortices are toroidal in shape before the 2-D–3-D transition. At a critical value of the Reynolds number they acquire circumferentially periodic oscillations in the axial direction and alternate periodically in crossing the axial midplane to invade the opposite half of the interdisk space. Humphrey et al. [8] showed that such an isothermal 3-D flow displayed a shift-and-reflect symmetry with respect to the interdisk midplane.

Figs. 5(a–d) show the cross-stream flow and the corresponding temperature distribution at two (z, r) planes located at $\theta = 0$ and $\theta = \pi/4$, for a 3-D calculation with $S = 0.091$, $Re = 20{,}565$ and $\varepsilon = 0.1$. This calculation, carried out on a $40 \times 74 \times 84$ (z, r, θ) grid, was started from the ending point of the corresponding isothermal calculation [1], where a quasi-periodic flow with circumferential wave-number $m = 4$ was obtained. The plot in Fig. 5(a) provides a picture of the instantaneous cross-stream flow at a θ location corresponding to a maximum negative axial velocity in the interdisk midplane at $r' = 0.80$. In the isothermal case, the cross-stream pattern at the (z, r) plane with $\theta = \pi/4$ would be the mirror reflection, with respect to the axial midplane, of that shown in Fig. 5(a) [8]. This is not the case for the present non-isothermal flow. As shown in Fig. 5(b), because centrifugal buoyancy favors the cross-stream circulation in the upper vortex, the symmetry properties with respect to the midplane are lost.

The respective temperature distributions are shown in Figs. 5(c) and (d). These plots suggest that the outflows along the disk Ekman layers are responsible for most of the heat transfer between disks. The isotherms are comparatively closer near the disk surface in those

regions of stronger radial outflow. The hot (up) and cold (down) flows along the enclosure wall meet at a certain point and a high rate of heat transfer is attained across the inwards jet between cross-stream vortices for $r' > 0.90$, as reflected by the close isotherms in Figs. 5(c) and (d). The corresponding plot of the isotherms in the (θ, r) plane, not shown here, is in agreement with the local Nusselt number distribution

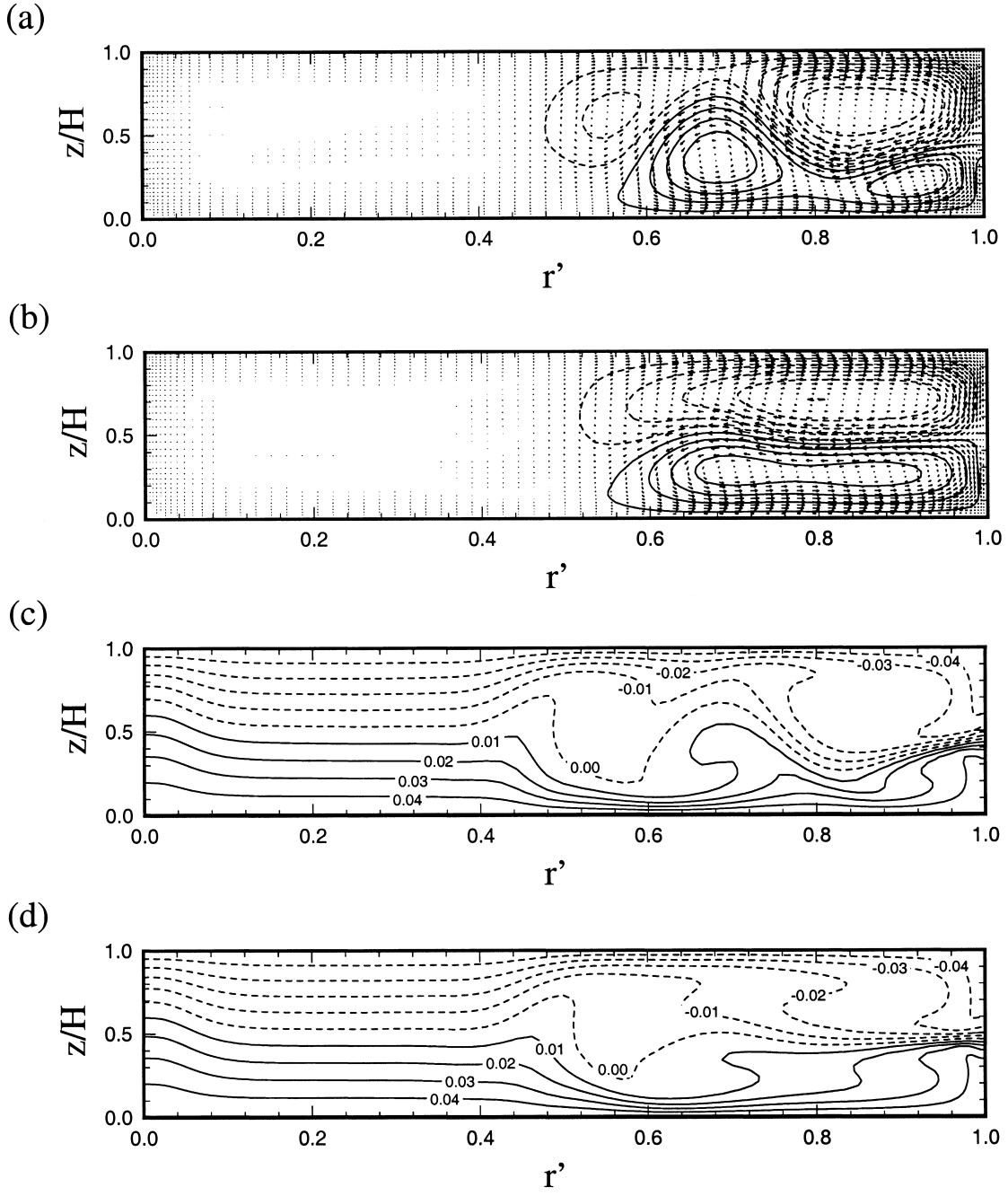

Fig. 5. Three-dimensional calculation of the flow for $Re = 20{,}565$, $S = 0.091$ and $\varepsilon = 0.1$ on a $40 \times 74 \times 84$ (z, r, θ) grid. Velocity vectors and streamlines, based on the axial and radial velocity components only, are shown in (a) and (b) for two cross-stream (z, r) planes with $\theta = 0$ and $\theta = \pi/4$, respectively. The corresponding distributions of the dimensionless temperature, $T' = (T - T_0)/(T_b - T_t)$, are, respectively, shown in (c) and (d).

given in Fig. 8(a). This is discussed in Section 4.5, where the relation between the 3-D structure of the flow and the overall heat transfer rates is explained.

In the isothermal case, fluid in the inner core, the region with $r' \leqslant 0.5$ for $S=0.091$, was observed to rotate as a solid body with the disks and hub [8]. The isotherms in Figs. 5(c) and (d) are slightly compressed upwards close to the hub, thus suggesting the presence of some cross-stream motion within the inner core. Such a circulation is attributed to centrifugal buoyancy but exerts very little influence on the overall heat transfer rate. Fig. 6 shows the axial profiles of the three (circumferentially averaged) velocity components at the radial location with $r'=0.30$. The profiles in Fig. 6 are almost identical to those reported in [11] for the case of circulation induced by centrifugal buoyancy inside a rotating cavity. Far away from solid boundaries, departures from solid body rotation within the inner core are insignificant, both in the averaged and in the local fields. Also in agreement with previous work, peak values of v and w in the profiles at $r' < 0.4$ scale well with $\Omega R^2\varepsilon$. Thus, in Figs. 5(a) and (b) the cross-stream motion near the enclosure wall is, on average, $1/\varepsilon$ times stronger than in the inner core.

4.4. Forced convection regime: asymmetrical flows

The isothermal ECDP flows investigated by Humphrey et al. [8] correspond to a unique interdisk spacing to disk radius ratio, namely $S=0.091$. For this aspect ratio, transition from a 2-D-steady into a 3-D-unsteady, isothermal ECDP flow always occurs through a Hopf bifurcation yielding a flow of the type discussed in Section 4.3. Iglesias and Humphrey [23] have recently shown that, when a higher geometry ratio value of $S=0.137$ is considered for the ECDP geometry of Fig. 1, a pitchfork bifurcation between two different types of isothermal, axisymmetric, steady flows is detected in 2-D calculations. The 2-D flow resulting from such a bifurcation displays a strong breaking of symmetry with respect to the interdisk midplane, meaning that one of the toroidal cross-stream vortices becomes considerably larger than the other (see Fig. 8 in [23]). Iglesias and Humphrey [23] also reported that such an asymmetrical or symmetry-breaking ECDP flow was not realizable in 3-D calculations. Notwithstanding, the present authors have shown [1] that an isothermal symmetry-breaking 3-D ECDP flow is attainable at the higher aspect ratio of

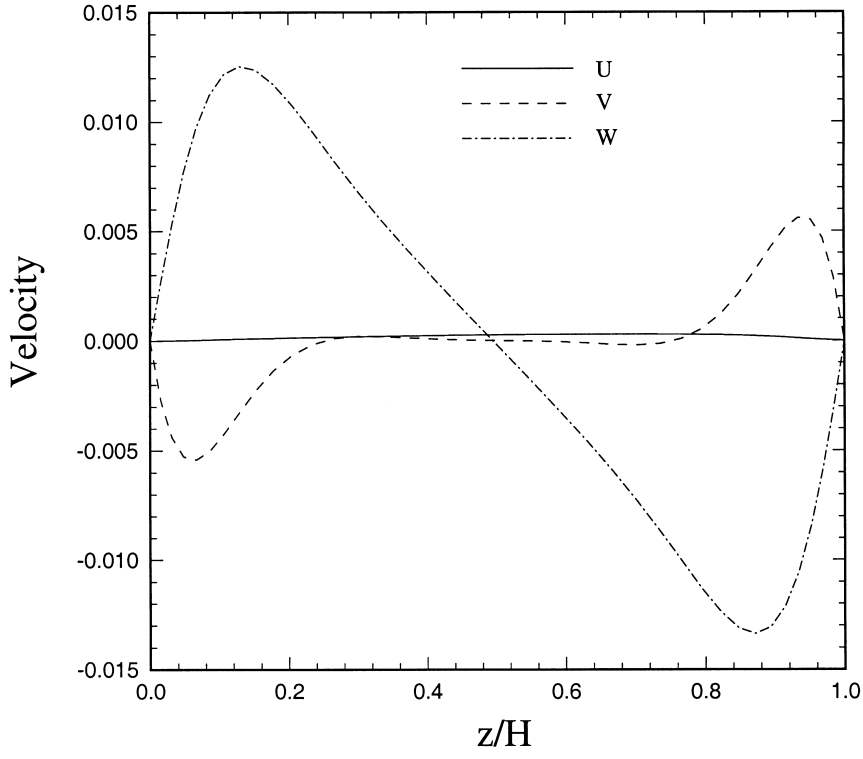

Fig. 6. Axial profiles of the circumferentially averaged velocity components at $r'=(r-R_1)/(R_2-R_1)=0.30$ for the same 3-D calculation as in Fig. 5. In this plot velocity is non-dimensionalized according to Eq. (3).

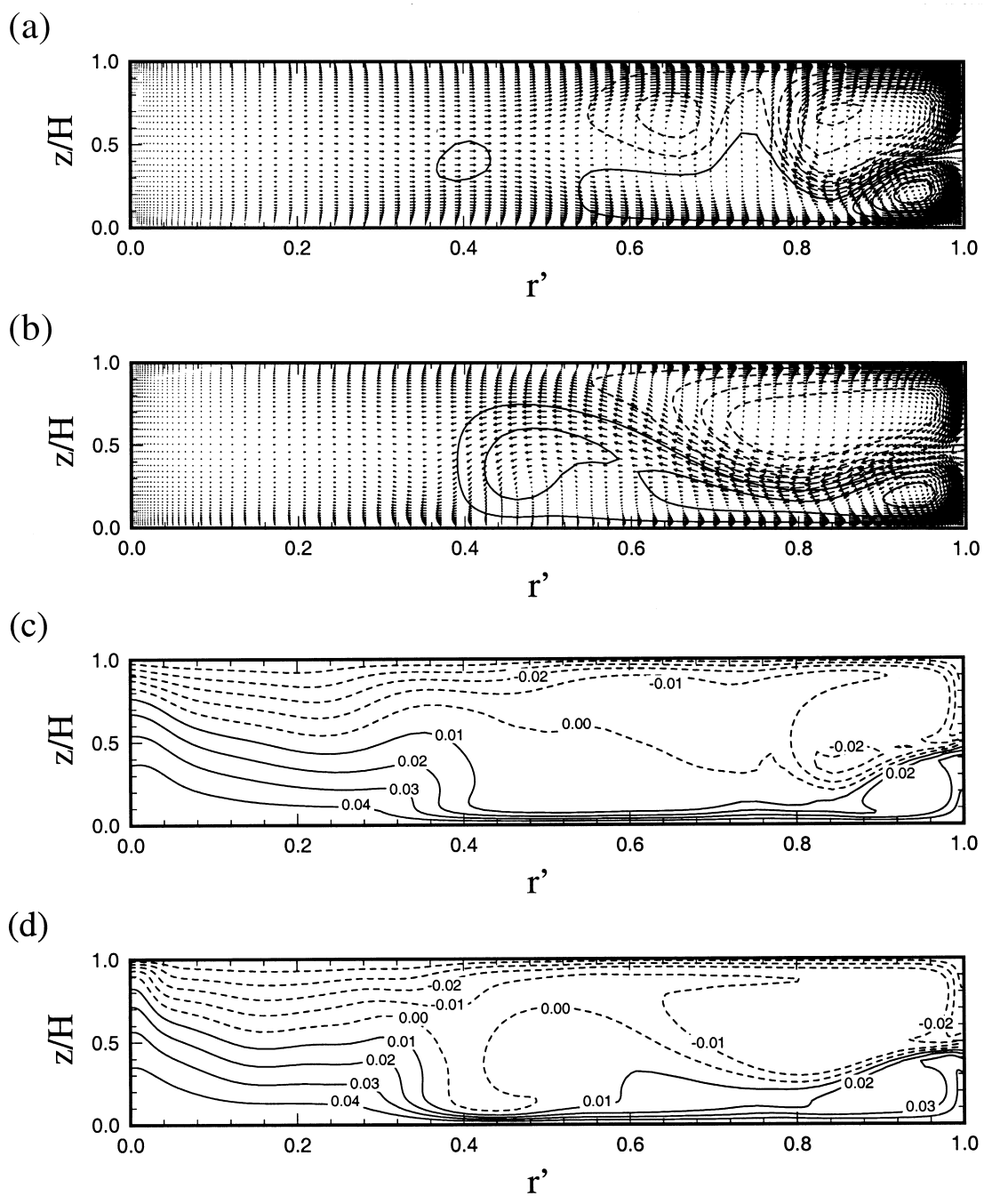

Fig. 7. Three-dimensional calculation for $Re=82{,}270$, $S=0.091$ and $\varepsilon=0.1$ on a $50\times90\times84$ (z, r, θ) grid. Velocity vectors and streamlines, based on the axial and radial velocity components only, are shown in (a) and (b) for two cross-stream (z, r) planes with $\theta=0$ and $\theta=7\pi/32$, respectively. The corresponding dimensionless temperature distributions are respectively shown in (c) and (d). Temperature is non-dimensionalized as in Fig. 5.

$S=0.18$. In the present non-isothermal case, the symmetry-breaking 3-D ECDP flow is also the preferred structure for $S=0.18$ at high enough Reynolds numbers. As is the case in the 2-D–3-D Hopf bifurcation at lower values of S, it has been found that the presence of centrifugal buoyancy does not significantly alter the location of the boundary for the 2-D–3-D transition at $S=0.18$. Interestingly, a new flow bifur-

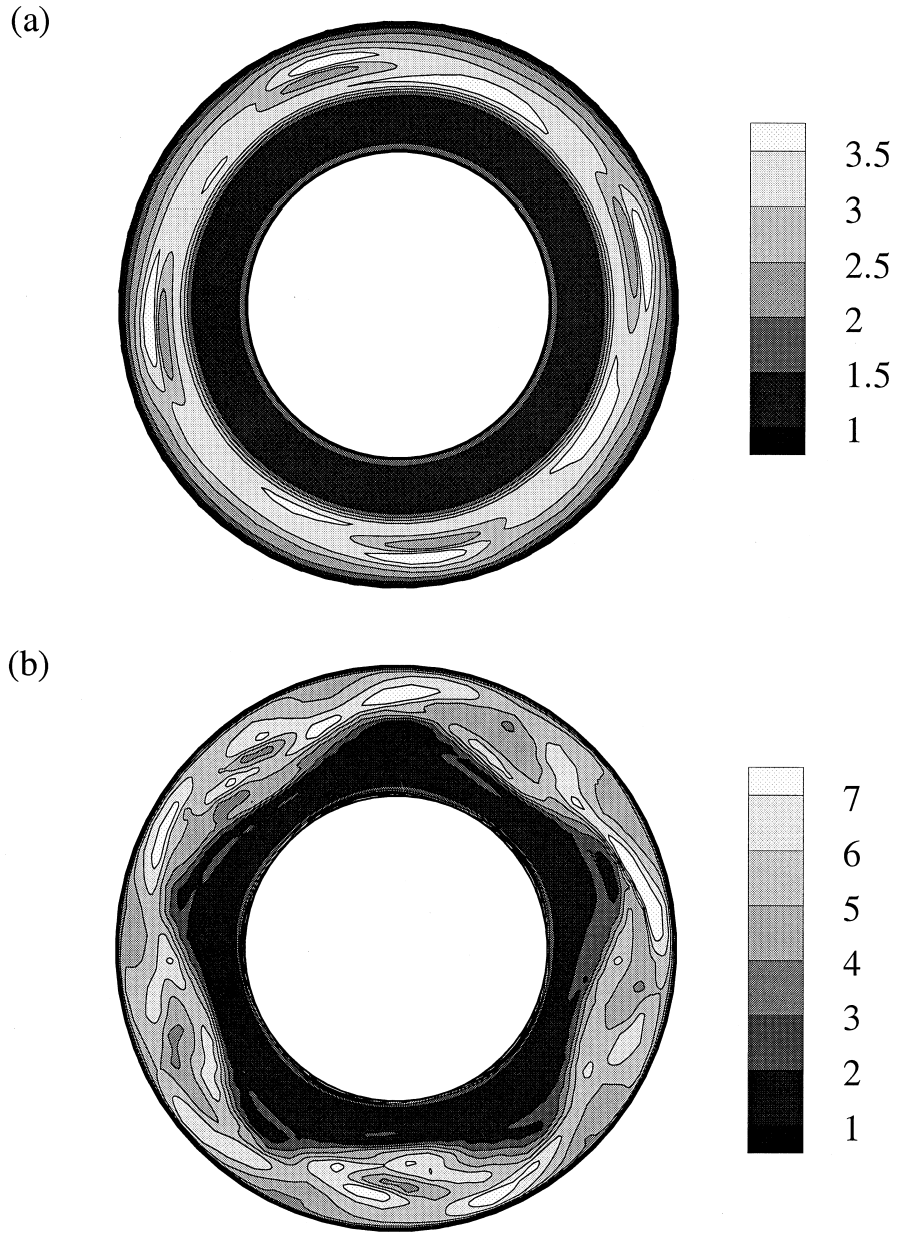

Fig. 8. Distribution of the local Nusselt number, defined in Eq. (11), along the top disk surface for the 3-D calculations of Figs. 5 and 7.

cation has been detected in the present calculations. It consists of a transition, after an increase in Re, from a 3-D flow as that of Section 4.3 towards a different type of 3-D flow displaying all of the characteristics of the isothermal symmetry-breaking 3-D ECDP flow reported in [1]. It is remarkable that such a 3-D–3-D flow bifurcation is not detected in the isothermal case. This means that the non-isothermal 3-D ECDP flow of the 'symmetry-breaking' type is stable at values of the [Re, S] pair where the corresponding isothermal symmetry-breaking 3-D flow is not.

For illustration, an example is given for the case with $Re = 82{,}270$, $\varepsilon = 0.1$ and the same value of $S = 0.091$ as in Section 4.3 to facilitate a proper comparison. For this set of parameters, a 3-D flow of the 'symmetry-breaking' type is obtained regardless of the initial conditions and history of the calculation. Figs. 7(a) and (b) show the cross-stream motion at two

different (z, r) planes, namely with $\theta=0$ and $7\pi/32$, for a 3-D calculation on a $50\times90\times84$ (z, r, θ). The flow in this case evolves on its own to attain a circumferential periodicity with $m=5$. The plots in Figs. 7(a) and (b) illustrate one of the main features of symmetry-breaking type ECDP flows. This is the presence of inflows and outflows between the outer region and the inner core. This type of ECDP flow features a third, highly 3-D, intermediate region between the inner core and the pair of counter-rotating cross-stream vortices [1]. In those θ-locations with the strongest radial outflows, as in Fig. 7(a), the ECDP vortices are compressed against the enclosure wall. The opposite is true in situations with strong radial inflows, as can be seen in Fig. 7(b). The above characteristics of the flow are reflected in the respective cross-stream temperature distributions, shown in Figs. 7(c) and (d). Such an alternating shrinking and enlargement of the ECDP cross-stream vortices has an effect on the overall heat transfer rates, as discussed below. The corresponding plot of the isotherms in the (θ, r) plane, not shown here, is in agreement with the local Nusselt number distribution given in Fig. 8(b), discussed below.

4.5. Heat transfer rates

The overall instantaneous rate of heat transfer between the two disks is calculated by integrating the local rate of heat transfer over either disk surface. This results in the instantaneous surface averaged Nusselt number, $\overline{Nu}$, given by

$$\overline{Nu}=\frac{\int_{\theta=0}^{\theta=2\pi}\int_{r=R_1}^{r=R_2}Nu(\theta,r)r\,\mathrm{d}r\,\mathrm{d}\theta}{\pi(R_2^2-R_1^2)}. \tag{10}$$

In this expression we imply the following relationships:

$$Nu(\theta,r)=\frac{h(\theta,r)H}{k};\quad h(\theta,r)=\frac{q(\theta,r)}{T_S(\theta,r)-T_0};\qquad q(\theta,r)=-k\left(\frac{\partial T(\theta,r)}{\partial z}\right)_S \tag{11}$$

where Nu and q are the instantaneous local values of the Nusselt number and heat flux, respectively, h is the instantaneous local heat transfer coefficient and T_S denotes the temperature at the disk surface, set as a constant in the present study. Note that the above expression for Nu is based on the characteristic length H, the interdisk spacing. In those calculations yielding a steady flow, the $\overline{Nu}$ values calculated for the bottom and the top disk surfaces are identical at all times. This is not the case when the flow is unsteady. However, time-averaged values of $\overline{Nu}$ for the two surfaces are very close, with differences less than 1% attributed to the finite length of the instantaneous $\overline{Nu}$ time records.

The question arises concerning how the values of $\overline{Nu}$ obtained by the above procedure should scale with Re and Pr for ECDP flows. This is related to the well-known case of heat/mass transfer from a free rotating disk for which Levich [24] published a theory in 1942. In this theory, which is based on boundary layer assumptions, the idea is that the disk radius-based local Nusselt number, Nu_r, can be expressed as

$$Nu_r=hr/k=f(Pr)\,Re_r^{0.5} \tag{12}$$

where Re_r denotes the local Reynolds number based on the radial location r and $f(Pr)$ is a function given by $f(Pr)=0.62Pr^{1/3}$, valid only in the limit of high Prandtl numbers. Several refinements to Levich's high Prandtl limit solution were later introduced by, among others, Sparrow and Gregg [25], Kreith et al. [26] and Newman [27], and a comprehensive review of work prior to 1966 is given by Ridford [28]. For the range of Prandtl numbers explored in this work, we use the more general equation for $f(Pr)$ derived analytically by Liu and Stewart [29]

$$f(Pr)=\frac{Pr^{1/3}}{\left(1.61173+\dfrac{0.4803}{Pr^{1/3}-0.4870}\right)};\qquad Pr^{1/3}\geq0.4870 \tag{13}$$

which is consistent with Levich's asymptote for very large values of Pr. Based on the above Eqs. (12) and (13), a scale for the local Nusselt number as a function of Pr and Re in ECDP flows may be accordingly expressed as follows:

$$Nu\propto f(Pr)S\,Re^{0.5}. \tag{14}$$

Note that the aspect ratio S appears in Eq. (14) because the Nusselt number is based on the interdisk spacing, H. The bulk temperature, T_0, is used here instead of the fluid temperature outside the boundary layer, as is usually the case in free-rotating disk flows. A further refinement has been introduced to obtain the corresponding scale for the surface averaged Nusselt number, $\overline{Nu}$. Eq. (10) is used to obtain the average value of Nusselt over the whole disk surface, that is, $R_1\leqslant r\leqslant R_2$. However, not all of the disk surface is useful from the point of view of heat transfer, as illustrated in Fig. 8(a) where the distribution of the Nusselt number on the top disk surface is plotted for the same 3-D calculation as in Fig. 5. As might be anticipated from Figs. 5(c) and (d), high local rates of heat transfer between the disk surface and the fluid are restricted to the outer part of the radial domain. The contribution from the inner core, with local values of

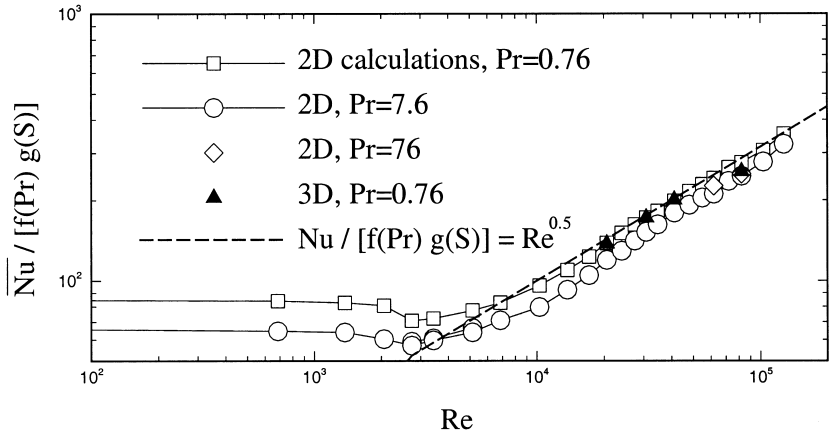

Fig. 9. Dependence of the calculated Nusselt numbers on Re and Prandtl for the ECDP geometry with $S=0.091$. The dashed line corresponds to the analytical scale based on the theory [24] of the rotating disk electrode. See the text for details.

Nusselt even lower than the $Nu=1$ limit for pure conduction, is almost negligible when the ECDP flow fully attains the forced convection regime. Therefore, the following scaling for $\overline{Nu}$ is proposed:

$$\overline{Nu} \propto f(Pr)g(S)\, Re^{0.5} \tag{15}$$

where $g(S)$ represents S times the ratio between the effective heat transfer area and the total disk surface equal to $\pi(R_2^2-R_1^2)$. Such a ratio has been included in the $g(S)$ part of the scale because one can expect [1,23] its value to increase with the geometry aspect ratio S. Eq. (15) is applicable to Reynolds numbers corresponding to the forced convection regime and is restricted to isothermal disks.

A rough estimation for $g(S)$, namely $g(S)=0.5\ S$, works well in Fig. 9 for ECDP flows with $S=0.091$. The $Re^{0.5}$ asymptote is well reproduced in this plot when the forced convection regime is fully attained. Note that the 2-D–3-D flow transition, detected at about $Re=16{,}000$ for the non-symmetry breaking flow conditions of Fig. 5, does not produce any noticeable break or change in the slope of the heat transfer curve in Fig. 9. Also, the value of $\overline{Nu}$ [see Eq. (10)] for the flow of Fig. 5 is very similar to the corresponding value obtained from a 2-D calculation. It is also clear

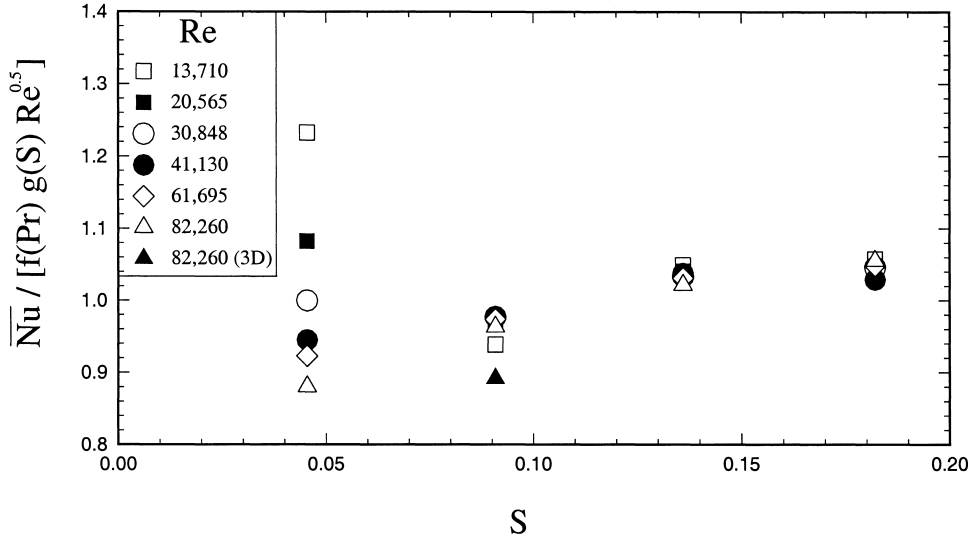

Fig. 10. Variation of the predicted Nusselt number with the interdisk height to radius aspect ratio, S, and the Reynolds number, Re, for the forced convection regime. The results in this plot correspond to $Pr=0.76$. Note the collapse of the data for all values of Re when $S>0.091$.

in Fig. 9 that Eq. (13) gives a fairly good prediction of the dependence of $\overline{Nu}$ on Pr for ECDP flows within the forced convection regime. It must be mentioned that while most calculations in this figure correspond to cases with $\varepsilon = 0.1$, runs at $Pr = 76$ were carried out with a smaller ε value, $\varepsilon = 0.01$, in order to rule out the presence of free convection in calculations within the Re range of interest, $10^4 < Re < 10^5$. It has been observed that, as a general rule, the presence of moderate centrifugal buoyancy in ECDP flows leads, within the forced convection regime, to an increase in $\overline{Nu}$ by a factor of roughly $(1+\varepsilon)$ between the $\varepsilon = 0$ limit and the maximum $\varepsilon = 0.1$ investigated in the present study.

It is not easy to establish a suitable general function for $g(S)$ in Eq. (15). This is illustrated in Fig. 8(b) for the 3-D calculation discussed in relation to Fig. 7 above. The Nu distribution at the top disk surface presents a pentagonal shape. As shown in [1], the polygonal shape of the inner core is characteristic of the 'symmetry-breaking' 3-D ECDP flows. The radial outflows and inflows, respectively, portrayed in Figs. 7(a) and (b) give the pentagonal shape to the inner core in Fig. 8(b). Because of the significant change in the effective heat transfer area with respect to that of Fig. 8(a), the predicted $\overline{Nu}$ value for the 3-D calculation of Fig. 8(b) is about 10% lower than the one obtained in the corresponding 2-D run. Thus, a $g(S)$ value that is suitable for the 'wavy' ECDP flow discussed in Section 4.3 is not appropriate for the 'symmetry-breaking' 3-D flow of Section 4.4.

Several calculations at different values of S and $Pr = 0.76$ have been performed to further investigate the effect of the geometry on the heat transfer rates. Calculations corresponding to $S = 0.18$ were carried at $\varepsilon = 0.01$ to make sure that free convection was absent in the Re range of interest. Results in Fig. 10 show that the asymptotic behavior $Re^{0.5}$ is attained at any S value when the Reynolds number is high enough.

5. Conclusions

The flow and heat transfer between a pair of disks corotating in a fixed cylindrical enclosure have been investigated. Attention has been given first to an analysis of the different physical phenomena and flow regimes that can arise depending on the dominant terms in the conservation equations. Results reported here illustrate the different transitions that are observed as the rotation speed of the disks is progressively increased.

The discussion then focused on the differences between isothermal and non-isothermal ECDP flows. The distinction between two types of 3-D ECDP flow also holds for the non-isothermal flow. For the type of flow of Section 4.3, previously investigated in the isothermal case by Humphrey et al. [8], centrifugally-induced buoyancy favors clockwise-rotating cross-stream cells and opposes anticlockwise-rotating ones, thus breaking the midplane shift-and-reflect symmetry of the isothermal flow. It is important to note, however, that such flow is still different from the type of 3-D ECDP flow previously labeled by the authors, for the isothermal-case, as 'symmetry-breaking'. The ECDP flow of the 'symmetry-breaking' type, discussed in Section 4.4, acquires a highly complex 3-D structure and features a much larger departure from midplane symmetry properties than that of Section 4.3.

It has also been shown that a transition between the two types of 3-D ECDP flows, already suggested in [1] but not numerically detected in the isothermal case, is realizable in the presence of moderate levels of centrifugal buoyancy. Such a different behavior between isothermal and non-isothermal 3-D ECDP flows is explained as follows. A 3-D isothermal ECDP flow of the shift-and-reflect or 'wavy' type [8] features a circumferential alternation of regions where cross-stream motion in the upper-half dominates that in the lower half, and vice versa. It is therefore difficult for such a 3-D flow to shift into a structure where either the lower or the upper cross-stream vortex, depending on the branch of the bifurcation selected, dominates the cross-stream motion over the whole θ-range. In the non-isothermal 'wavy' flow case discussed in Section 4.3, the upper cross-stream toroidal vortex, favored by centrifugal buoyancy, dominates the lower one. This makes the bifurcation into the 'symmetry-breaking' type of 3-D ECDP flow discussed in Section 4.4 much easier.

The prediction of heat transfer rates between disks, a subject of practical interest, has also been analyzed. Using existing theory for the heat and mass transfer from a freely rotating disk, a proper scaling for Nu as a function of both Re and Pr has been proposed for the case when the ECDP system operates within the forced convection regime. It has been shown that, in many cases, good predictions of the Nusselt number may be obtained by performing 2-D (axisymmetric flow) calculations. However, when the 3-D ECDP flow is not 'wavy' but of the 'symmetry-breaking' type, intensive 3-D calculations are necessary to guarantee accurate predictions of the overall heat transfer rates between disks.

Acknowledgements

The calculations for this study were initially performed on the CRAY supercomputers of the Cray Research Center at Minnesota, through a grant received by F. Giralt from Cray Inc. Additional calculations were performed on the CRAY EL-94 of the

ETSEQ in Tarragona and in the Thermofluids Laboratory of the Department of Mechanical Engineering of the University of California at Berkeley using a RISC 6000 provided by IBM to J. A. C. Humphrey under the auspices of the Computer Mechanics Laboratory. Financial support for J. Herrero while at the University of California at Berkeley was provided by the C.I.R.I.T. (Generalitat de Catalunya). Financial support was awarded to F. Giralt by the Dirección General de Investigación Científica y Técnica (DGICYT). Part of the research was financially supported by the DGICYT projects PB93-0656-C02-01 and PB96-1011. These sources of funding are gratefully acknowledged.

References

[1] J. Herrero, F. Giralt, J.A.C. Humphrey, Influence of geometry on the structure of the flow between a pair of corotating disks, Phys. Fluids 11 (1999) 88–96.
[2] J.M. Owen, R.H. Rogers, Flow and heat transfer in rotating disc systems. Volume 2, rotating cavities, in: Mechanical engineering research studies: engineering design series, Wiley, New York, 1995.
[3] J.W. Chew, Computation of convective laminar flow in rotating cavities, J. Fluid Mech. 153 (1985) 339–360.
[4] D. Bohn, E. Deuker, R. Emunds, V. Gorzelitz, Experimental and theoretical investigations of heat transfer in closed gas filled rotating annuli, J. Turbomachinery 117 (1995) 11–19.
[5] D. Bohn, R. Emunds, V. Gorzelitz, U. Kruger, Experimental and theoretical investigations of heat transfer in closed gas filled rotating annuli, J. Turbomachinery 118 (1996) 175–183.
[6] C.A. Schuler, B. Usry, B. Weber, J.A.C. Humphrey, R. Greif, On the flow in the unobstructed space between shrouded corotating disks, Phys. Fluids A 2 (1990) 1760.
[7] J.A.C. Humphrey, Ch-J Chang, H. Li, C.A. Schuler, Unobstructed and obstructed rotating disk flows: a summary review relevant to information storage systems, Adv. Info. Storage Syst. 1 (1991) 79.
[8] J.A.C. Humphrey, C.A. Schuler, D. Webster, Unsteady laminar flow between a pair of disks corotating in a fixed cylindrical enclosure, Phys. Fluids 7 (1995) 1225.
[9] E.L. Koschmieder, Bénard cells and Taylor vortices, in: Cambridge monograph series on mechanics and applied mathematics, Cambridge University Press, Cambridge, New York, 1993.
[10] S. Chandrasekhar, Hydrodynamic and Hydromagnetic Stability, Clarendon Press, Oxford, 1961.
[11] J. Herrero, J.A.C. Humphrey, F. Giralt, Comparative analysis of coupled flow and heat transfer between corotating disks in rotating and fixed cylindrical enclosures, in: M.K. Chyu, N.V. Nirmalan (Eds.), Heat Transfer in Gas Turbines, vol. HTD-300, American Society of Mechanical Engineers, 1994, pp. 111–121.
[12] D.D. Gray, A. Giorgini, The validity of the Boussinesq approximation for liquids and gases, Int. J. Heat Mass Transfer 19 (1976) 545–551.
[13] J. Frölich, P. Laure, R. Peyret, Large departures from Boussinesq approximation in the Rayleigh–Bénard problem, Phys. Fluids A 4 (1992) 1335–1372.
[14] K. Tatsutani, W.R. Usry, J.A.C. Humphrey, Numerical calculation of two-dimensional laminar flow and heat transfer for a backward-facing step using Cuteflows, in: B. Blackwell, D.W. Pepper (Eds.), Benchmark Problems for Heat Transfer Codes, vol. HTD-222, ASME Winter Annual Meeting, Anaheim, California, 1992, pp. 1–6.
[15] I. Iglesias, J.A.C. Humphrey, F. Giralt, Numerical calculation of two-dimensional buoyancy-assisted flow past a backward-facing step in a vertical channel, in: B.F. Blackwell, B.F. Armally (Eds.), Computational Aspects of Heat Transfer, Benchmark Problems, vol. HTD-258, ASME Winter Annual Meeting, New Orleans, Louisiana, 1993, pp. 63–72.
[16] Davis G. De Vahl, Natural convection of air in a square cavity: a bench mark numerical solution, Int. J. Numer. Methods Fluids 3 (1983) 249–264.
[17] J.C. Buell, I. Catton, The effect of wall conduction in the stability of a fluid in a right circular cylinder heated from below, J. Heat Transfer 105 (1983) 255–260.
[18] E.L. Koschmieder, S.G. Pallas, Heat transfer through a shallow horizontal convecting fluid layer, Int. J. Heat Mass Transfer 17 (1974) 991–1002.
[19] E.L. Koschmieder, On convection on a uniformly heated rotating plane, Beitr. Phys. Atmos. 40 (1967) 216–225.
[20] A. Schüler, D. Luntz, F. Busse, On the stability of steady finite amplitude convection, J. Fluid Mech. 23 (1965) 129–144.
[21] G.M. Homsy, J.L. Hudson, Centrifugal convection and its effect on the asymptotic stability of a bounded rotating fluid heated from below, J. Fluid Mech. 48 (1971) 605–624.
[22] P.G. Daniels, The effect of centrifugal acceleration on axisymmetric convection in a shallow rotating cylinder or annulus, J. Fluid Mech. 99 (1980) 65–84.
[23] I. Iglesias, J.A.C. Humphrey, Two- and three-dimensional laminar flows between disks co-rotating in a fixed cylindrical enclosure, Int. J. Numer. Methods Fluids 26 (1998) 581–603.
[24] V.G. Levich, Physicochemical Hydrodynamics, Prentice-Hall, Englewood Cliffs, NJ, 1962.
[25] E.M. Sparrow, J.L. Gregg, Heat transfer from a rotating disk to fluids of any Prandtl number, ASME J. Heat Transfer 81 (1959) 249–251.
[26] F. Kreith, J.H. Taylor, J.P. Chong, Heat and mass transfer from a rotating disk, ASME J. Heat Transfer 81 (1959) 95–105.
[27] J. Newman, Current distribution on a rotating disk below the limiting current, J. Electrochem. Soc. 113 (1966) 1235–1241.
[28] A.C. Ridford, The rotating disk system, Advances in Electrochemistry and Electrochemical Engineering 4 (1966) 47–116.
[29] K.T. Liu, W.E. Stewart, Asymptotic solutions for forced convection from a rotating disk, Int. J. Heat Mass Transfer 15 (1972) 187–189.